PAPER

Free-standing graphene-based nanohybrid paper electrode as an anode for lithium-ion batteries

Young Soo Yun and Hyoung-Joon Jin*

In this study, a free-standing nanohybrid paper electrode (F-Nanohybs) was prepared using nitrogen-doped graphene-based nanosheets (N-GNSs) and mesoporous Mn_3O_4 nanoparticles (M-Mn_3O_4). N-GNSs had a thickness of ~3 nm and a nitrogen content of 5.3%. M-Mn_3O_4 had a highly crystalline, mesoporous structure with surface area of 60 $m^2\ g^{-1}$. F-Nanohybs electrodes were produced *via* simple vacuum filtration of a homogeneous dispersion of N-GNS and M-Mn_3O_4. The F-Nanohybs exhibited a good electrical conductivity (5.4 S cm^{-1}), large specific surface area (151 $m^2\ g^{-1}$), and a well-organized morphology. Thus, the F-Nanohybs displayed a high reversible capacity of (740 mA h g^{-1}) at a current density of 100 mA g^{-1} and a stable performance over 100 consecutive charge/discharge cycles.

Introduction

The design of nanostructured electrode materials has been extensively studied in order to produce high-performance power sources.[1,2] At the nanometer scale, a large increase in the surface-to-volume ratio occurs, leading to changes in local material properties; thus, research in areas such as nanoionics and nanoelectronics has been accelerated due to breakthroughs in the design of nanostructured materials for energy storage devices.[3,4] Of the existing nanostructured materials, graphene, a new class of two-dimensional carbon nanostructures, has attracted great interest on account of its unique properties such as high electron mobility (15 000 $cm^2\ V^{-1}\ s^{-1}$) and large surface area (2600 $m^2\ g^{-1}$).[5,6] Graphene nanosheets, when used as an anode material for lithium-ion batteries (LIBs), exhibit high reversible capacity, exceptional rate capability, and good cycle performance; moreover, the electrochemical performance is improved on doping with nitrogen atoms.[7–11]

Meanwhile, the use of free-standing paper electrodes is advantageous in many respects, as it eliminates the need for binders such as polyvinylidene fluoride, conducting agents, and current collectors such as copper (~10 mg cm^{-2}) and aluminum (5 mg cm^{-2}).[12,13] Thus, the use of free-standing paper electrodes can increase the practical energy density. However, a more sophisticated electrode design is required to achieve power characteristics and cycle performances comparable to those of conventional electrodes, wherein the graphene sheets are packed in a more disordered manner. Graphene-based paper electrodes exhibit superior flexibility owing to strong interactions between graphene nanosheets; this property enables the application of flexible power sources to a large variety of

products such as roll-up displays, wearable devices, and other soft portable electronic products. However, at the same current density, a well-stacked graphene paper electrode shows a lower reversible capacity (84 mA h g^{-1} at 50 mA g^{-1}) compared to that of a conventional powder electrode (288 mA h g^{-1} at 50 mA g^{-1}).[14] This difficulty can be alleviated by doping the graphene-based paper electrode with a metal oxide.[15–18] Nanohybrids based on synthesized graphene nanosheets and metal oxide nanoparticles are not only easy to prepare but also exhibit substantially improved electrochemical performance.[19–24] Graphene nanosheets in the nanohybrid provide electron conduction pathways and facilitate fast ionic diffusion for the metal oxide, apart from functioning as a buffer by restraining cyclic pulverization of the metal oxide due to volume expansion/extraction. Synergistic effects of the nanohybrids are dependent on their nanostructures, and therefore, more research is required to produce well-defined, improved nanostructures.

In this study, free-standing nanohybrid electrodes (F-Nanohybs) based on nitrogen-doped graphene-based nanosheets (N-GNSs) and mesoporous Mn_3O_4 nanoparticles (M-Mn_3O_4) are prepared by simple vacuum filtration, and their performance as an anode material for LIBs is investigated in terms of their electrochemical properties.

Experimental

Preparation of N-GNSs

Graphene oxide (GO) powder was prepared using a previously reported method.[6,25] A dispersion of GO powder in water, with a concentration of 0.5 mg mL^{-1} was prepared by ultrasound treatment. Melamine monomer (Sigma-Aldrich) was then added to the GO dispersion with vigorous stirring until it was completely dissolved. The GO–melamine solution (GO–melamine weight ratio of 1 : 2) was frozen in liquid nitrogen and

Department of Polymer Science and Engineering, Inha University, Incheon 402-751, South Korea. E-mail: hjjin@inha.ac.kr

subsequently freeze-dried using a lyophilizer (LP3, Jouan, France) at -50 °C and 4.5 Pa for 72 h. After lyophilization, a low-density, loosely packed melamine-adsorbed GO powder was obtained. The powder was heated in a tubular furnace from room temperature to 600 °C at a rate of 10 °C min^{-1}, under an Ar flow rate of 200 mL min^{-1}. The reaction mixture was held at this temperature (600 °C) for 2 h. The resulting product was stored in a vacuum oven at 30 °C.

Preparation of M-Mn₃O₄

The M-Mn₃O₄ nanoparticles were prepared by template-free self-assembly under ultrasound sonication.[26] 2.8 mL of 4 M H₂SO₄ was added dropwise to 100 mL of 0.1 M KMnO₄ with constant stirring; following 5 min of ultrasound treatment, this solution was centrifuged and decanted. The resulting supernatant solution was rapidly injected by a syringe to 400 mL of 0.02 M MnSO₄ under constant ultrasound sonication for 30 min; subsequently, the mixture was vigorously stirred for 3 h at room temperature. The as-prepared product was vacuum-filtered and washed with ethanol and deionized water, followed by heating in a tubular furnace from room temperature to 400 °C at a heating rate of 5 °C min^{-1}. The reaction mixture was held at this temperature (400 °C) for 2 h.

Preparation of F-Nanohybs

10 mg each of N-GNSs and M-Mn₃O₄ was separately dispersed in dimethylformamide by ultrasound treatment. The N-GNS and M-Mn₃O₄ dispersions were then mixed with vigorous stirring. After stirring for 30 min, the N-GNS/M-Mn₃O₄ dispersion mixture was vacuum-filtered on an alumina template membrane. The product (F-Nanohybs) was dried in a vacuum oven at 30 °C and peeled off from the alumina template membrane.

Characterization

The morphology of the N-GNSs and M-Mn₃O₄ nanostructures was studied using field-emission transmission electron microscopy (FE-TEM; JEM2100F, JEOL, Japan). The surface and fracture surface morphologies of F-Nanohybs were characterized using field-emission scanning electron microscopy (FE-SEM; S-4300, Hitachi, Japan). XRD (Rigaku DMAX 2500) analysis of the N-GNSs and M-Mn₃O₄ nanostructures was performed using Cu K$_\alpha$ radiation (wavelength $\lambda = 0.154$ nm) operating at 40 kV and 100 mA. A continuous-wave linearly polarized laser with a wavelength of 473 nm (2.62 eV), a pinhole of 50 μm, and a 600 grooves per mm grating was used for Raman spectroscopy. To ensure nondestructive measurements, a low laser power (<300 μW, on the sample) was used. The porosity of M-Mn₃O₄ was determined from nitrogen adsorption/desorption isotherms, which were obtained using a surface area and porosimetry analyzer (ASAP 2020, Micromeritics, USA) at -196 °C. X-ray photoelectron spectroscopic analysis (XPS, PHI 5700 ESCA) was performed using monochromatic Al K$_\alpha$ radiation ($h = 1486.6$ eV). Fourier transform infrared spectroscopy (FT-IR) was performed using VERTEX 80v (Bruker Optics, Germany). The electrical properties of the samples were characterized using an electrical conductivity meter (Loresta GP, Mitsubishi Chemical, Japan).

Electrochemical performance was evaluated using a Wona-tec automatic battery cycler and CR2016-type coin cells. The working electrodes were prepared by punching the F-Nanohybs and N-GNSs without using any binder or substrate. The coin cells were assembled in an argon-filled glove box. A composite electrode with metallic lithium foil was used as the cathode and 1 M LiPF₆ (Aldrich, purity: 99.99%) dissolved in a solution of ethylene carbonate–dimethyl carbonate (1 : 1 v/v) served as the electrolyte. The cells were galvanostatically cycled between 0.01 and 3.0 V vs. Li/Li$^+$ at various current densities.

Results and discussion

The morphology of the N-GNSs was studied using FE-TEM, as shown in Fig. 1a and b. The planar nanosheets have a rough surface with a thickness of ~3 nm, and are composed of ~10 stacked graphene layers. During heat treatment, oxygen groups on the GO are eliminated due to the desorption of some isolated epoxy groups and by the release of CO₂ and CO, thus reducing the GO.[24] This leads to vacancy defects and nanoscale holes on
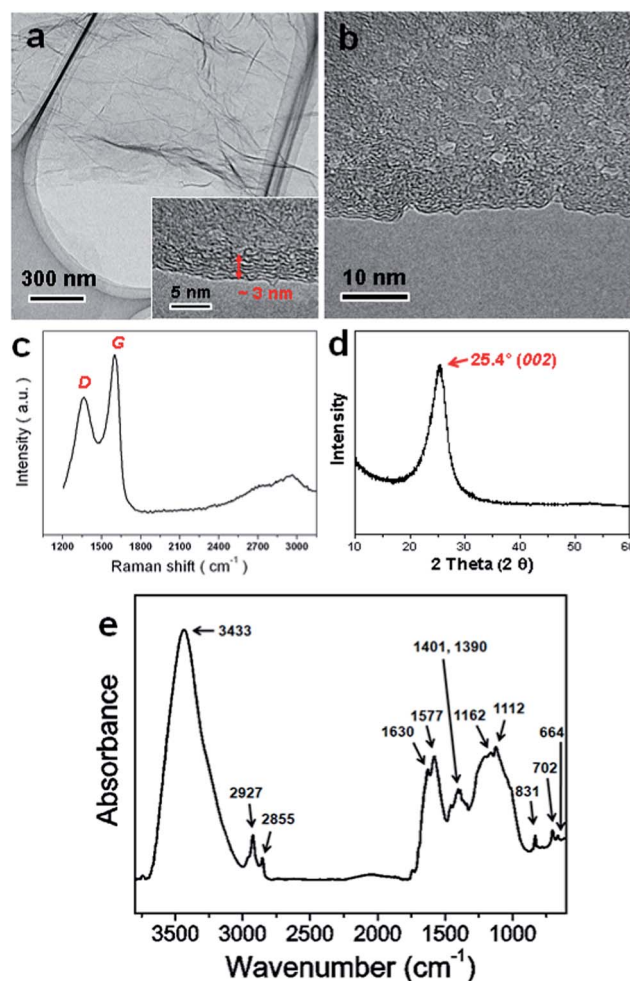

Fig. 1 (a) and (b) FE-TEM images of N-GNSs at different magnifications. (c) Raman data and (d) XRD data of N-GNSs. (e) FT-IR spectrum of N-GNS.

the surface of the N-GNS.[27,28] The rough surface of the N-GNSs can be attributed to the vacancy defects or the nanoscale holes. The Raman spectroscopy data show a relatively high G band intensity-to-D band intensity ratio (I_G/I_D ratio = 1.37). The presence of the D peak points to defects in the ideal graphene structure, which break the symmetry of the infinite carbon honeycomb lattice. In contrast, the G peak originates from the doubly degenerate E_{2g} phonon at the Brillouin zone center. Thus, a higher I_G/I_D ratio is indicative of a well-developed graphitic structure. The XRD data of the N-GNSs show a distinct diffraction peak at 25.4°, corresponding to the (002) plane of graphite. The height (L_c) of the graphitic layers calculated from the (002) peak is about 2.7 nm, which agrees with the value obtained from FE-TEM. These results suggest that the inner layers of the N-GNSs have well-developed graphitic structures, in contrast to the defective surface.

Chemical configurations of the N-GNSs were investigated by FT-IR spectroscopy. The bands at 2927 and 2855 cm^{-1} corresponded to the CH_2 stretching vibration, while C=C groups were identified by bands at 1577 and 1630 cm^{-1}. Peaks indicating the presence of oxygen functional groups such as O–H, epoxide, C–O–C, and C–O are observed at 3433, 1401, 1390, 1162, and 1112 cm^{-1}, respectively. Further, peaks indicating the presence of heterocyclic compounds such as pyridine derivatives or pyrimidines are observed at 831, 702, and 664 cm^{-1}. These results show that a variety of nitrogen-containing functional groups are present in the N-GNSs. The XPS data also support this claim. In the XPS C 1s spectrum of the N-GNSs, several distinct peaks (C–O and C–N centered at 285.8 eV, and C(O)O centered at 290.2 eV) were found, including a main C–C peak at 284.7 eV (Fig. 2a).[29–31] The nitrogen atoms in the N-GNSs are mostly in the form of pyridine and pyridone, as indicated by the N 1s peak centered at 398.2 and 400.3 eV, respectively, which is characteristic of a six-membered ring at the edge of a graphene sheet (Fig. 2b).[29–31] Additionally, two distinct peaks (531.9 and 533.5 eV) in the O 1s spectrum indicated the presence of oxygen atoms in the form of carbonyl groups as well as other oxygen-containing groups (Fig. 2c).[29–31] The nitrogen and oxygen contents of the N-GNSs were found to be 5.3% and 10.1%, respectively. The nitrogen doping process by melamine molecules is postulated to occur as follows: melamine molecules are adsorbed on the GO surface through π–π interactions and hydrogen bonding. During heat treatment, the nitrogen-containing functional groups of the melamine molecules react with the oxygen-containing functional groups or defect sites of the GO and/or are condensed into carbon nitride on the surface of the GO.[32] The nitrogen-doping process thus incorporates thermally stable aromatic structures such as six-membered rings (pyridine and pyridone) onto the surface of the GO. A mixed phase of rGO and char containing nitrogen groups could be formed as a by-product of this process.

M-Mn$_3$O$_4$ nanoparticles produced by a rapid synthetic method have diameters of approximately 400 nm, and are composed of numerous spherical nanoparticles (Fig. 3a). The primary nanoparticles are highly crystalline with diameters of ~20 nm (Fig. 3b–d). Nitrogen adsorption/desorption isotherms of M-Mn$_3$O$_4$ show an IUPAC type-IV shape with an H1-type
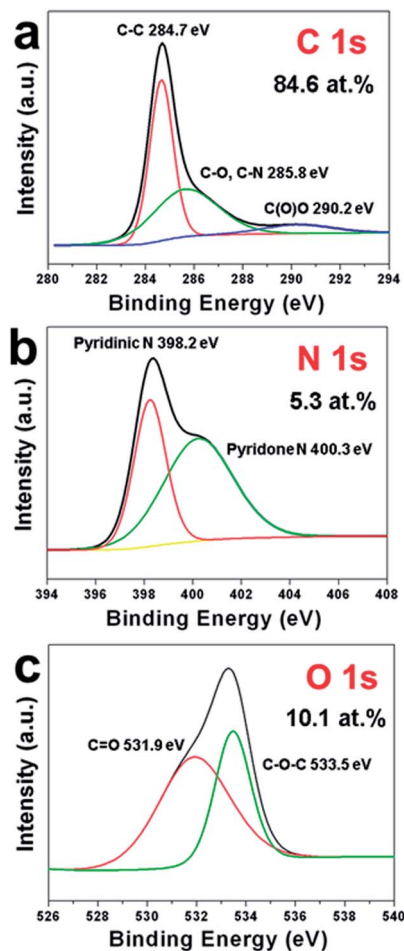

Fig. 2 XPS (a) C 1s, (b) N 1s, and (c) O 1s spectra of N-GNSs.

hysteresis loop, indicating a mesoporous structure. The H1-type hysteresis loop is shown by agglomerates or compacts of approximately uniform spheres in a fairly regular array. This indicates that the aggregated primary nanoparticles of M-Mn$_3$O$_4$ have a uniform size and result in mesoporous structures. Pore sizes in the M-Mn$_3$O$_4$ nanostructure range from 5 to 35 nm, and the mean pore size is approximately 15 nm. The specific surface area of Mn$_3$O$_4$ is 60 m^2 g^{-1}.

The F-Nanohybs samples were prepared by simple vacuum filtration of the N-GNS/M-Mn$_3$O$_4$ dispersion mixture. The F-Nanohybs exhibited an extremely rough surface morphology, and M-Mn$_3$O$_4$ was well dispersed between the stacked edge sites of the N-GNSs (Fig. 4a). This is in contrast to the well-stacked morphology of the N-GNSs (Fig. 4b).

The fracture surface images indicate that the thickness of F-Nanohybs is ~30 μm and that M-Mn$_3$O$_4$ is homogeneously distributed in the loosely packed layers of N-GNS (Fig. 4c and d). The F-Nanohybs exhibited a good electrical conductivity (5.4 S cm^{-1}), similar to that of free-standing N-GNS papers (6.3 S cm^{-1}) in the absence of M-Mn$_3$O$_4$. This suggests that the electrical pathways of F-Nanohybs are well developed and are unaffected by the M-Mn$_3$O$_4$ components. The F-Nanohybs were punched and used as anode material without the use of binder and substrate.
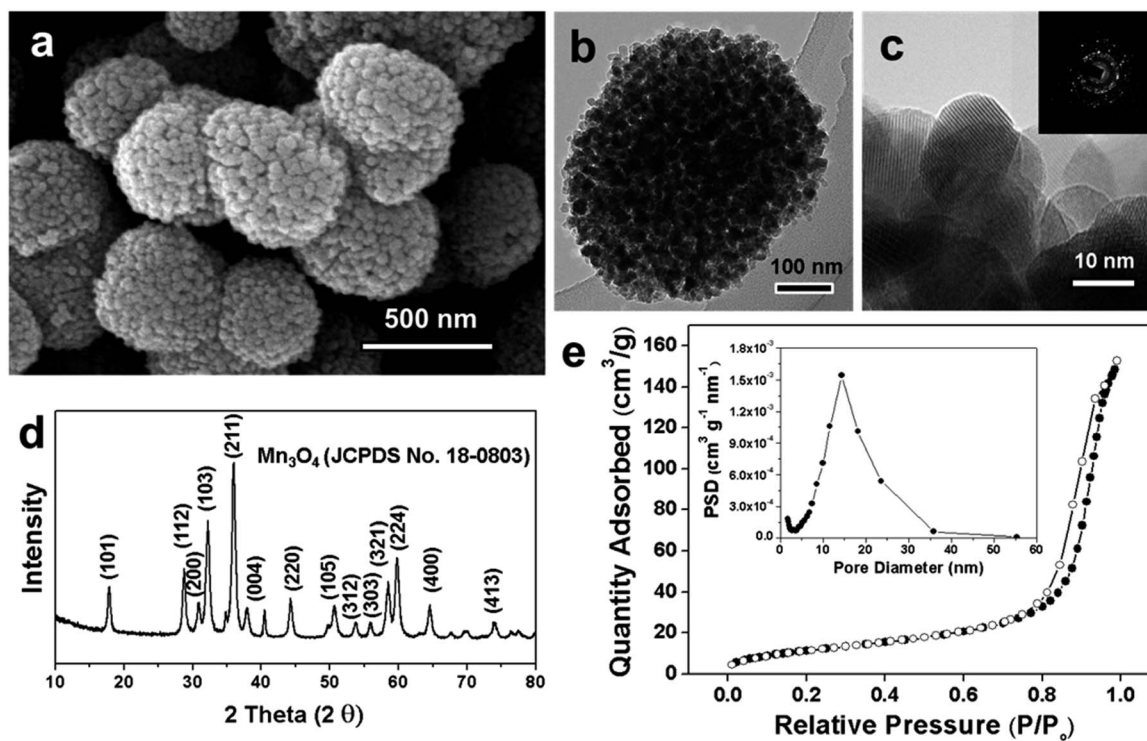
Fig. 3 (a) SEM image of M-Mn₃O₄; (b) and (c) FE-TEM images at different magnifications. (d) XRD data of M-Mn₃O₄. (e) Nitrogen adsorption/desorption isotherms of M-Mn₃O₄ and pore size distribution of M-Mn₃O₄ (inset of e).
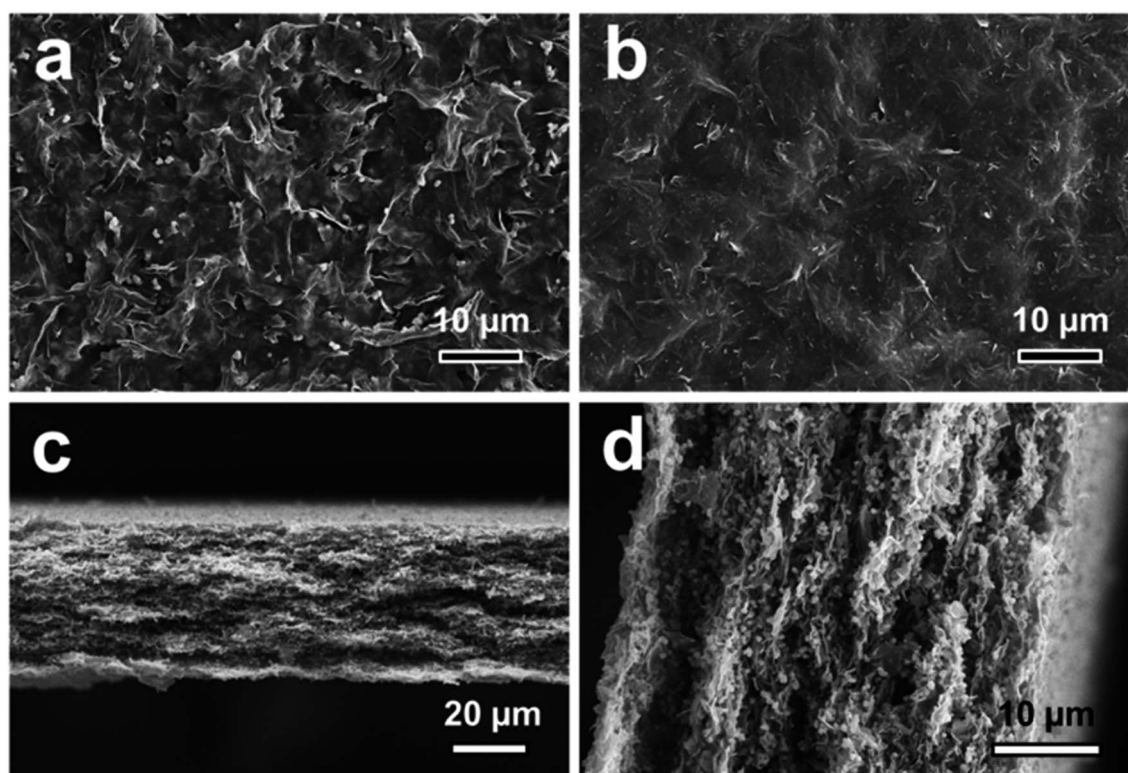

Fig. 4 SEM images of the surface of (a) F-Nanohybs and (b) N-GNS; (c) and (d) cross section of F-Nanohybs at different magnifications.

The nitrogen adsorption/desorption isotherms of F-Nanohybs show an IUPAC type-IV mesoporous structure, with an H2-type hysteresis loop, indicating a poorly defined pore structure (Fig. 5). The pore size distribution of the F-Nanohybs shows that a large number of pores are present, in a broad size range from 10 to 1000 nm. The specific surface area of the F-Nanohybs is 151 m^2 g^{-1}, which is 2.5 times that of Mn_3O_4 (60 m^2 g^{-1}); thus, the F-Nanohybs exhibit a porous internal structure with a large specific surface area in spite of their free-standing paper shapes.

The electrochemical performance of F-Nanohybs, N-GNSs, and M-Mn_3O_4 was investigated by a half cell test using Li-metal as the reference electrode. The cells were galvanostati-cally cycled between 0.01 and 3.0 V at various current densities (Fig. 6). The M-Mn_3O_4-based electrode was prepared by mixing the active material (80 wt%) with conductive carbon (10 wt%) and polyvinylidene fluoride (10 wt%) in N-methyl-2-pyrrolidone. The resulting slurry was uniformly applied to the Cu foil. The F-Nanohybs displayed a large first discharge capacity of 1650 mA h g^{-1} after several Li-ion storage steps. The voltages between 1 and 0.4 V can be attributed to electrolyte decomposition and the formation of a solid electrolyte interface (SEI) film on the elec-trode surface (Fig. 6a). The subsequent plateau and continuous voltage drop in the potential range of 0.4–0.1 V can be attributed to Li-ion storage in M-Mn_3O_4, and N-GNS, respectively. The first reversible capacity of F-Nanohybs (740 mA h g^{-1}) was 4 times that of N-GNSs (180 mA h g^{-1}), and a similar charge profile with a slight decrease in the capacity was shown in subsequent cycles, thus demonstrating the reversible Li-ion storage behavior of F-Nanohybs. The high reversible capacity of F-Nanohybs surpasses the average of the reversible capacities of N-GNSs and M-Mn_3O_4.

Thus, it can be concluded that the improved performance of N-GNS/M-Mn_3O_4 composites is due to synergistic effects. M-Mn_3O_4 introduced in the stacked graphene layers of N-GNSs creates numerous crevices between the layers; therefore, the composite has a greater number of active sites in comparison to the N-GNSs. In addition, the N-GNSs provide electrical pathways
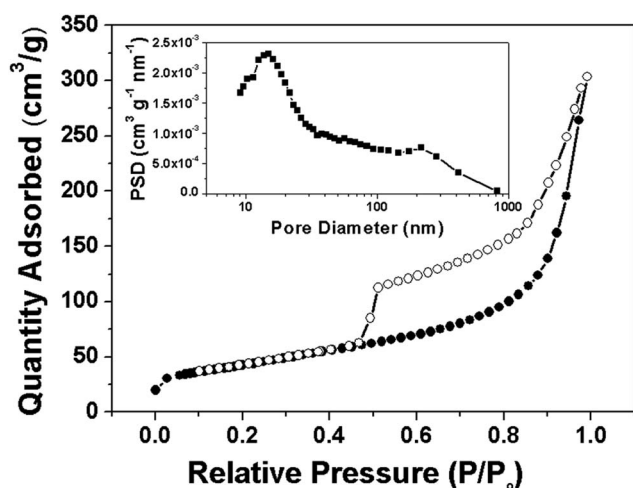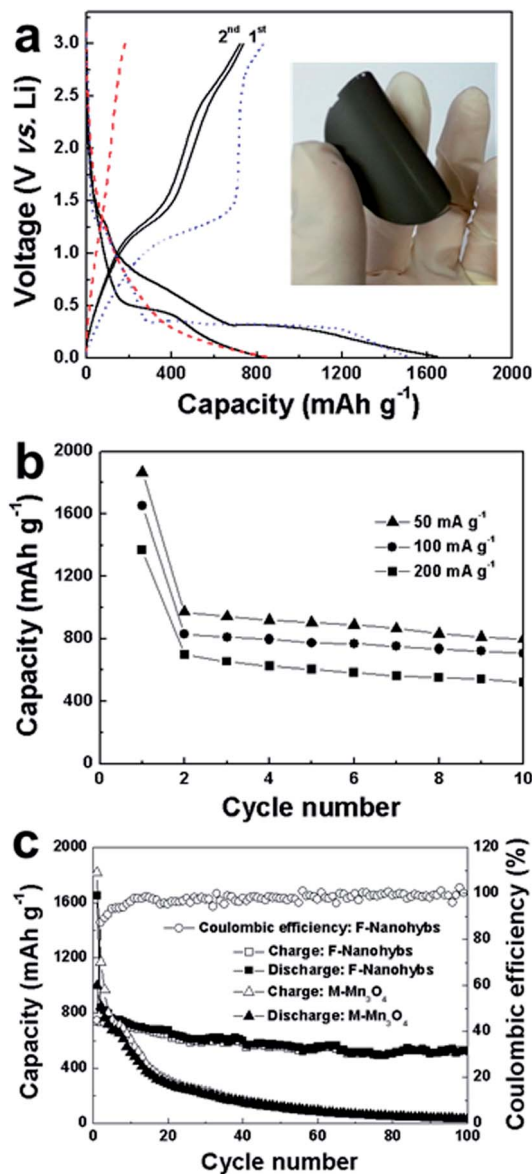

Fig. 6 Electrochemical performance of F-Nanohybs, N-GNSs, and M-Mn_3O_4 in an electrolyte of 1 M LiPF$_6$ dissolved in ethylene carbonate–dimethyl carbonate (1 : 1 v/v). (a) Galvanostatic charge/discharge profiles of the first and second cycles of F-Nanohybs (black, solid), the first cycles of N-GNSs (red, dash), and M-Mn_3O_4 (blue, dot) between 0.1 to 3 V vs. Li at a current density of 100 mA g^{-1}. (b) Rate capability of F-Nanohybs at different current densities such as 50, 100 and 200 mA g^{-1}. (c) Cyclic performance of F-Nanohybs and M-Mn_3O_4 at a current density of 100 mA g^{-1}.

to M-Mn_3O_4 and therefore, M-Mn_3O_4 is fully utilized for Li-ion storage.

The Li-ion storage performance was investigated at different current densities such as 50, 100, and 200 mA g^{-1} (Fig. 6b). After two consecutive charge/discharge cycles, specific capacities of 968, 807, and 690 mA h g^{-1} were obtained at current densities of 50, 100, and 200 mA g^{-1}, respectively. For a fourfold increase in current density, a specific capacity of about 71% is maintained; a similar drop in capacity is observed over ten consecutive charge/discharge cycles. These results indicate that F-Nanohybs

Fig. 5 Nitrogen adsorption/desorption isotherms and pore size distribution curve (inset) of F-Nanohybs.

shows good rate performance. The cyclic performance of F-Nanohybs and M-Mn$_3$O$_4$ was investigated over 100 consecutive charge/discharge cycles at a current density of 100 mA g^{-1} (Fig. 6c). After 100 cycles, F-Nanohybs had a specific capacity of 527 mA h g^{-1} with nearly 100% Coulombic efficiency. In contrast, M-Mn$_3$O$_4$ showed a rapid drop in capacity with each consecutive cycle. After 20 cycles, M-Mn$_3$O$_4$ had a capacity of about 300 mA h g^{-1}, and a much lower capacity of 34 mA h g^{-1} was maintained after 100 cycles. The excellent electrochemical performance and stable charge/discharge cycles of F-Nanohybs can be attributed to the well-organized composite structure and the synergistic effects of N-GNSs/M-Mn$_3$O$_4$.

Conclusions

F-Nanohybs was fabricated by simple vacuum filtration from nanostructured components, *viz.* N-GNS and M-Mn$_3$O$_4$. N-GNS had a thickness of ∼3 nm and a rough surface with an abundance of heteroatoms such as nitrogen (5.3%) and oxygen (10.1%). M-Mn$_3$O$_4$ had a diameter of approximately 400 nm and was composed of highly crystalline primary particles with diameters of ∼20 nm. Further, M-Mn$_3$O$_4$ had a mesoporous structure with a surface area of 60 m^2 g^{-1}. F-Nanohybs, a composite of N-GNSs and M-Mn$_3$O$_4$, exhibited a good electrical conductivity (5.4 S cm^{-1}), large specific surface area (151 m^2 g^{-1}), and homogeneous distribution of M-Mn$_3$O$_4$ in the stacked graphene layers of N-GNSs. Thus, F-Nanohybs exhibits a high reversible capacity (740 mA h g^{-1}), good rate performance, and stable cyclic performance with nearly 100% Coulombic efficiency as an anode material for LIBs.

Acknowledgements

Notes and references

1 A. S. Aricò, P. Bruce, B. Scrosati, J.-M. Tarascon and W. V. Schalkwijk, *Nat. Mater.*, 2005, **4**, 366.
2 Y.-G. Guo, J.-S. Hu and L.-J. Wan, *Adv. Mater.*, 2008, **20**, 2878.
3 J. Maier, *Nat. Mater.*, 2005, **4**, 805.
4 W. Lu and C. M. Lieber, *Nat. Mater.*, 2007, **6**, 841.
5 K. S. Novoselov, A. K. Geim, S. V. Morozov, D. Jiang, M. I. Katsnelson, I. V. Grigorieva, S. V. Dubonos and A. A. Firsov, *Nature*, 2005, **438**, 197.
6 Y. S. Yun, Y. H. Bae, D. H. Kim, J. Y. Lee, I.-J. Chin and H.-J. Jin, *Carbon*, 2011, **49**, 3553.
7 G. Wang, X. Shen, J. Yao and J. Park, *Carbon*, 2009, **47**, 2049.
8 H. Wang, C. Zhang, Z. Liu, L. Wang, P. Han, H. Xu, K. Zhang, S. Dong, J. Yao and G. Cui, *J. Mater. Chem.*, 2011, **21**, 5430.
9 X. Li, D. Geng, Y. Zhang, X. Meng, R. Li and X. Sun, *Electrochem. Commun.*, 2011, **13**, 822.
10 A. L. M. Reddy, A. Srivastava, S. R. Gowda, H. Gullapalli, M. Dubey and P. M. Ajayan, *ACS Nano*, 2010, **4**, 6337.
11 Z.-S. Wu, W. Ren, L. Xu, F. Li and H.-M. Cheng, *ACS Nano*, 2011, **5**, 5463.
12 Y. S. Yun, M. E. Lee, M. J. Joo and H.-J. Jin, *J. Power Sources*, 2014, **246**, 540.
13 Y. S. Yun, J. M. Kim, H. H. Park, J. Lee, Y. S. Huh and H.-J. Jin, *J. Power Sources*, 2013, **244**, 747.
14 A. Abouimrane, O. C. Compton, K. Amine and S. T. Nguyen, *J. Phys. Chem. C*, 2010, **114**, 12800.
15 J. Liang, Y. Zhao, L. Guo and L. Li, *ACS Appl. Mater. Interfaces*, 2012, **4**, 5742.
16 R. Wang, C. Xu, J. Sun, L. Gao and C. Lin, *J. Mater. Chem. A*, 2013, **1**, 1794.
17 S. Liu, R. Wang, M. Liu, J. Luo, X. Jin, J. Sun and L. Gao, *J. Mater. Chem. A*, 2014, **2**, 4598.
18 T. Hu, X. Sun, H. Sun, M. Yu, F. Lu, C. Liu and J. Lian, *Carbon*, 2013, **51**, 322.
19 X. Wang, X. Zhou, K. Yao, J. Zhang and Z. Liu, *Carbon*, 2011, **49**, 133.
20 X. Zhu, Y. Zhu, S. Murali, M. D. Stoller and R. S. Ruoff, *ACS Nano*, 2011, **5**, 3333.
21 Y. Su, S. Li, D. Wu, F. Zhang, H. Liang, P. Gao, C. Cheng and X. Feng, *ACS Nano*, 2012, **6**, 8349.
22 H. Wang, L.-F. Cui, Y. Yang, H. S. Casalongue, J. T. Robinson, Y. Liang, Y. Cui and H. Dai, *J. Am. Chem. Soc.*, 2010, **132**, 13978.
23 S. Mao, Z. Wen, H. Kim, G. Lu, P. Hurley and J. Chen, *ACS Nano*, 2012, **6**, 7505.
24 Y. Sun, X. Hu, W. Luo, F. Xia and Y. Huang, *Adv. Funct. Mater.*, 2013, **23**, 2436.
25 Y. S. Yun, V.-D. Le, H. Kim, S.-J. Chang, S. J. Baek, S. Park, B. H. Kim, Y.-H. Kim, K. Kang and H.-J. Jin, *J. Power Sources*, 2014, **262**, 79.
26 J. M. Kim, Y. S. Huh, Y.-K. Han, M. S. Cho and H. J. Kim, *Electrochem. Commun.*, 2012, **14**, 32.
27 A. Bagri, C. Mattevi, M. Acik, Y. J. Chabal, M. Chhowalla and V. B. Shenoy, *Nat. Chem.*, 2010, **2**, 581.
28 K. Erickson, R. Erni, Z. Lee, N. Alem, W. Gannett and A. Zettl, *Adv. Mater.*, 2010, **22**, 4467.
29 Y. S. Yun, J. Shim, Y. Tak and H.-J. Jin, *RSC Adv.*, 2012, **2**, 4353.
30 Y. S. Yun, S. Y. Cho, J. Shim, B. H. Kim, S.-J. Chang, S. J. Baek, Y. S. Huh, Y. Tak, Y. W. Park, S. Park and H.-J. Jin, *Adv. Mater.*, 2013, **25**, 1993.
31 Y. S. Yun, C. Im, H. H. Park, I. Hwang, Y. Tak and H.-J. Jin, *J. Power Sources*, 2013, **234**, 285.
32 M. Groenewolt and M. Antonietti, *Adv. Mater.*, 2005, **17**, 1789.